The extended Baryon Oscillation Spectroscopic Survey: a cosmological forecast

Gong-Bo Zhao,[1,2]★ Yuting Wang,[1,2] Ashley J. Ross,[2,3] Sarah Shandera,[4,5] Will J. Percival,[2] Kyle S. Dawson,[6] Jean-Paul Kneib,[7,8] Adam D. Myers,[9] Joel R. Brownstein,[6] Johan Comparat,[10]† Timothée Delubac,[7] Pengyuan Gao,[1] Alireza Hojjati,[11,12] Kazuya Koyama,[2] Cameron K. McBride,[13] Andrés Meza,[14] Jeffrey A. Newman,[15] Nathalie Palanque-Delabrouille,[16] Levon Pogosian,[12] Francisco Prada,[10,17,18] Graziano Rossi,[19] Donald P. Schneider,[4,20] Hee-Jong Seo,[21] Charling Tao,[22,23] Dandan Wang,[1] Christophe Yèche,[16] Hanyu Zhang,[1] Yuecheng Zhang,[1] Xu Zhou,[1] Fangzhou Zhu[24] and Hu Zou[1]

Affiliations are listed at the end of the paper

ABSTRACT

We present a science forecast for the extended Baryon Oscillation Spectroscopic Survey (eBOSS) survey. Focusing on discrete tracers, we forecast the expected accuracy of the baryonic acoustic oscillation (BAO), the redshift-space distortion (RSD) measurements, the f_{NL} parameter quantifying the primordial non-Gaussianity, the dark energy and modified gravity parameters. We also use the line-of-sight clustering in the Lyman α forest to constrain the total neutrino mass. We find that eBOSS luminous red galaxies, emission line galaxies and clustering quasars can achieve a precision of 1, 2.2 and 1.6 per cent, respectively, for spherically averaged BAO distance measurements. Using the same samples, the constraint on $f\sigma_8$ is expected to be 2.5, 3.3 and 2.8 per cent, respectively. For primordial non-Gaussianity, eBOSS alone can reach an accuracy of $\sigma(f_{NL}) \sim 10$–15. eBOSS can at most improve the dark energy figure of merit by a factor of 3 for the Chevallier–Polarski–Linder parametrization, and can well constrain three eigenmodes for the general equation-of-state parameter. eBOSS can also significantly improve constraints on modified gravity parameters by providing the RSD information, which is highly complementary to constraints obtained from weak lensing measurements. A principal component analysis shows that eBOSS can measure the eigenmodes of the effective Newton's constant to 2 per cent precision; this is a factor of 10 improvement over that achievable without eBOSS. Finally, we derive the eBOSS constraint (combined with *Planck*, Dark Energy Survey and BOSS) on the total neutrino mass, $\sigma(\Sigma m_\nu) = 0.03$ eV (68 per cent CL), which in principle makes it possible to distinguish between the two scenarios of neutrino mass hierarchies.

Key words: dark energy – large-scale structure of Universe.

1 INTRODUCTION

The cosmic acceleration discovered at the end of last century is one of the most challenging problems to solve in modern science (Riess et al. 1998; Perlmutter et al. 1999). Possible solutions include introducing dark energy, a hypothetical new energy component in the Universe with a negative pressure (see Weinberg et al. 2013 for a recent review of dark energy), and modifying general relativity on cosmological scales (see Clifton et al. 2012 for a recent review).

The nature of dark energy and gravity remains unknown, but new observations can provide important information to reveal the underlying fundamental physics. For example, we can infer the nature of dark energy by probing its equation-of-state (EoS) $w(z)$, which is the ratio between its pressure and energy density, and is a function of redshift z in general. In the Λ cold dark model (ΛCDM) model, which is regarded as the standard cosmological

model, dark energy is assumed to be the vacuum energy with $w = -1$. Any deviation of w from -1, if revealed by observations, might suggest that the dark energy dynamically evolves with time, which will have a significant impact on many subjects in physics. The behaviour of w affects the expansion history of the Universe, thus it can be probed by distance measurements, such as those obtained by measuring the baryonic acoustic oscillations (BAO) signal imprinted on the galaxy clustering pattern on scales of about 150 Mpc. Modification of gravity (MG), on the other hand, can give rise to an accelerating Universe without dark energy. In this scenario, MG is predicted to alter the structure formation of the Universe. Thus, if one were to measure a scale-dependent growth pattern on sub-horizons scales, which is not present in general relativity (GR), it would be a 'smoking gun' for the discovery of MG. Thus the redshift-space distortions (RSD) signal (Kaiser 1987) measured by galaxy surveys is a powerful tool to test gravity.

Weighing neutrinos is one of the key science drivers of many high-energy experiments. However, due to the tiny cross-section of neutrinos, it is difficult for these experiments to measure the absolute mass of neutrinos. Instead, only the mass differences between neutrino species have so far been measured through neutrino oscillations. Latest measurements give the squared mass differences $\Delta m_{21}^2 = 7.53 \pm 0.18 \times 10^{-5}$ eV^2 and $\Delta m_{32}^2 = 2.44 \pm 0.06 \times 10^{-3}$ eV^2 for the normal mass hierarchy (NH; $m_3 \gg m_2 \simeq m_1$) and $\Delta m_{32}^2 = 2.52 \pm 0.07 \times 10^{-3}$ eV^2 for the inverted mass hierarchy (IH; $m_3 \ll m_2 \simeq m_1$; Olive & Particle Data Group 2014), where m_1, m_2 and m_3 denote the mass of three different species of neutrinos. Our Universe is an ideal laboratory to measure the total mass of neutrinos and distinguish between two mass hierarchies because massive neutrinos affect cosmological observables in significant ways. Existing in the form of radiation in the early Universe, neutrinos shift the epoch of the matter-radiation equality thus changing the shape of the cosmic microwave background (CMB) angular power spectrum. At late times, massive neutrinos can damp the formation of cosmic structure on small scales due to the free-streaming effect, thus affecting the cosmic growth factor, which can be probed by redshift surveys (Dolgov 2002; Lesgourgues & Pastor 2006).

Different inflation models predict varying levels of primordial non-Gaussianity (NG), so measuring the NG observationally can test our assumptions of the physical mechanism governing the early Universe. Primordial NG can change the clustering pattern of galaxies on large scales of the Universe through an induced large-scale bias (Dalal et al. 2008; Desjacques, Seljak & Iliev 2009). Therefore observing the large-scale clustering of galaxies can shed light on the physics in the early Universe.

The Baryon Oscillation Spectroscopic Survey (BOSS)[1] (Dawson et al. 2013), part of the Sloan Digital Sky Survey III (SDSS-III; Eisenstein et al. 2011), has observed spectra of more than 1.5 million galaxies brighter than $i = 19.9$ and approximately 170 000 new quasars of redshift $2.1 \leq 3.5$ to a depth of $g < 22$ (Paris et al., in preparation).[2] The precision of BAO and RSD measurements from Data Release 11 (DR11) of BOSS have been reduced to 1–2 and 6 per cent, respectively, and have provided stringent constraints on dark energy, modified gravity, neutrino mass, primordial NG and other cosmological parameters when combined with other observations (Ross et al. 2013; Zhao et al. 2013; Anderson et al. 2014; Beutler et al. 2014; Samushia et al. 2014; Palanque-Delabrouille et al. 2015a,b; Rossi et al. 2015).

The extended Baryon Oscillation Spectroscopic Survey (eBOSS) is a new redshift survey within SDSS-IV, observations for which started in 2014 July.[3] The eBOSS cosmology program uses the same 1000-fibre optical spectrographs installed on the 2.5-m-aperture Sloan Foundation Telescope (Gunn et al. 2006) at the Apache Point Observatory (APO) in New Mexico, used for the BOSS of SDSS-III. The eBOSS program will map the Universe over the redshift range $0.6 < z < 2.2$ by observing multiple tracers including luminous red galaxies (LRGs), emission line galaxies (ELGs) and quasars: a sample that combines eBOSS LRGs with the BOSS LRGs at $z > 0.6$ provides a 1 per cent distance measurement; the ELGs sample offers a 2 per cent estimate at slightly higher redshifts and the clustering quasars (CQs) produce a 1.6 per cent measurement in $0.9 < z < 2.2$ (Dawson et al. 2015).[4] These distance measurements are expected to improve the dark energy figure of merit (FoM; Albrecht et al. 2009) by a factor of 3 compared to BOSS results.

This paper presents the expected cosmological implications of the eBOSS survey including the BAO and RSD measurements and f_{NL} constraints, and is one of a series of technical papers describing the eBOSS survey. In Section 2, we describe the eBOSS survey in details. We outline the methodology used for the science forecasts for discrete tracers in Section 3. Our forecasts on cosmological parameters also include the expected BAO-scale precision from the 3D Lyman α (Lyα) forest clustering. We present the results in Section 4. Section 5 contains conclusions and discussions.

2 THE eBOSS SURVEY

The eBOSS survey is described in detail in Dawson et al. (2015), and we highlight the key facts here.

Motivated by the success of BOSS, eBOSS will extend the SDSS BAO measurement to $0.6 < z < 1$ using LRGs and ELGs, and make the first BAO measurement at $0.9 < z < 2.2$ using quasars.

The selected LRGs will cover the redshift range of $0.6 < z < 1$ over 7000 deg^2 with a surface number density of 50 deg^{-2}. We assume a bias model of $b(z)_{LRG} = 1.7 G(0)/G(z)$, where $G(z)$ is the linear growth factor at redshift z. Details of LRGs target selection are presented in Prakash et al. (2015).

The ELGs survey will start in Fall of 2016. The target selection definitions of the ELGs sample are not yet finalized and thus we explore three possible selection options, each of which will use some subset of the following imaging data: the South Galactic Cap U-band Sky Survey (SCUSS; Zhou et al. 2015; Zou et al. 2015),[5] Sloan Digital Sky Survey (SDSS) *griz* (Fukugita et al. 1996), *Wide-Field Infrared Survey Explorer* (*WISE*; Wright et al. 2010) or *grz* imaging with the Dark Energy Survey camera (DECam; Flaugher et al. 2015).[6] The proposed selections are the following.

---

[1] To avoid confusion with the numerous acronyms used in this work, we included a minidictionary in Table 1.

[2] More details of the BOSS filter, spectrograph and pipeline, see Fukugita et al. (1996), Smee et al. (2013) and Bolton et al. (2012).

[3] http://www.sdss.org/surveys/eboss/

[4] The clustering quasars provide a 2 per cent BAO distance measurement if 58 quasars per square degree over $0.9 < z < 2.2$ is assumed.

[5] For more information about the SCUSS survey, see http://batc.bao.ac.cn/Uband/

[6] Another option is mentioned in the eBOSS overview paper (Dawson et al. 2015), which only uses the *gri* and *Uri* bands of the SDSS and SCUSS imaging for target selection. We are not including it here because it produces tracers at low efficiency (only 52.5 per cent).

Table 1. The acronyms used in this work and their expression.

The acronym	The meaning
APO	Apache Point Observatory
BAO	Baryon acoustic oscillation
BOSS	Baryon Oscillation Spectroscopic Survey
CMB	Cosmic microwave background
CPL	Chevallier–Polarski–Linder
CQs	Clustering quasars
DECam	Dark Energy Survey camera
FoM	Figure of merit
DE	Dark energy
DES	Dark Energy Survey
DESI	Dark Energy Spectroscopic Instrument
DR	Data Release
eBOSS	extended Baryon Oscillation Spectroscopic Survey
ELGs	Emission line galaxies
EoS	Equation-of-state
FoG	Fingers-of-God
GR	General relativity
LRGs	Luminous red galaxies
MG	Modified gravity
NG	non-Gaussianity
RSD	Redshift-space distortion
SCUSS	South Galactic Cap U-band Sky Survey
SDSS	Sloan Digital Sky Survey
WISE	*Wide-Field Infrared Survey Explorer*
WL	Weak lensing

(i) *Fisher discriminant*. The targets are selected using the WISE, SDSS and SCUSS photometry with a cut on the Fisher discriminant quantities instead of cuts in the colour–colour diagrams (Raichoor et al. 2016). The initial tests of this scheme demonstrate its validity: it approaches the requirement that 74 per cent of targets turn out to be ELGs in the redshift range $0.6 < z < 1.0$ (henceforth referred to as the '74 per cent purity requirement'). We assume a completeness of 95 per cent over 1500 deg^2.

(ii) *Low-density DECam*. The targets are selected from DECam *grz* photometry. The deeper photometry means this selection exceeds the 74 per cent purity requirement for $0.7 < z < 1.1$. The expected target density is $\sim$190 deg^{-2}. The survey area is assumed to be 1400 deg^{-2}.

(iii) *High-density DECam*. The targets are selected in a similar way to the 'low density' case but the colour cuts are tuned to achieve a target density of $\sim$240 deg^{-2} over 1100 deg^{-2} (Dawson et al. 2015).

We assume a bias of $b(z)_{\mathrm{ELG}} = 1.0G(0)/G(z)$ for the ELGs (Dawson et al. 2015).

The clustering quasars will be targeted using the XDQSOz algorithm (Bovy et al. 2012), which was used for the quasar sample of BOSS, applied on the QSO_CORE sample in eBOSS. The expected number density to obtain 2 per cent precision on the BAO measurement over the redshift range $0.9 < z < 2.2$ is 58 deg^{-2} over an area of 7500 deg^2. This number is quoted as the base requirement for the CQs in Dawson et al. (2015) and Myers et al. (2015). In reality, the eBOSS selection approach detailed in Myers et al. (2015) exceeds this metric, successfully targeting closer to 70 deg^2 $0.9 < z < 2.2$ quasars over 7500 deg^2. In the rest of this paper (i.e. see Table 1), we adopt the redshift distribution corresponding to this expected quasar density of 70 deg^2 $0.9 < z < 2.2$ from Myers et al. (2015). This selection contains a useful tail of an additional $\sim$8 deg^{-2} quasars in the redshift range $0.6 < z < 0.9$, which we include in our forecasts

throughout the rest of this paper. Note that in Myers et al. (2015) the CQs are referred to as the QSO_CORE sample.

We assume the bias of the clustering quasars to be $b(z)_{\mathrm{CQ}} = 0.53 + 0.29(1 + z)^2$ (Croom et al. 2005; Ross et al. 2009). Table 2 summarizes the targets used in this work, including the number and volume number density of each type of targets in each redshift slice, the effective redshift, the total number of targets, the surface area and the bias. We follow Dawson et al. (2015) and take a conservative sky area for the LRGs to be 7000 deg^2 instead of 7500 deg^2. Different tracers overlap maximally in the survey area. Fig. 1 shows the redshift distribution we adopt for the tracers, where the overlap in redshifts is apparent. The time evolution of the biases is also shown.

3 METHODOLOGY

In this section, we present the methodology for the science forecast, which is based on the Fisher matrix technique (Tegmark, Taylor & Heavens 1997). The formalism is presented in Sections 3.1–3.5, and the parametrization and fiducial cosmology is shown in Section 3.6. We allow for the multitracer nature of eBOSS, including the cross-correlation when using the power spectra of different kinds of targets in overlapping regions of sky and in redshift.

3.1 The Fisher matrix for $P(k)$ of redshift surveys

Using the 3D galaxy power spectrum in redshift space measured from eBOSS, the Fisher matrix element for a pair of arbitrary parameters $\{p_i, p_j\}$ is given by (Tegmark 1997)[7]

$$F_{ij} = \frac{V_{\mathrm{sur}}}{4\pi^2} \int_{-1}^{1} \mathrm{d}\mu \int_{k_{\mathrm{min}}}^{k_{\mathrm{max}}} k^2 \mathrm{d}k \, \mathcal{F}_{ij}(k, \mu), \tag{1}$$

$$k_{\mathrm{min}} = \frac{2\pi}{V_{\mathrm{sur}}^{1/3}} \, [\mathrm{h\,Mpc^{-1}}], \quad k_{\mathrm{max}} = 0.1 \frac{D(0)}{D(z)} \, [\mathrm{h\,Mpc^{-1}}], \tag{2}$$

$$\mathcal{F}_{ij}(k, \mu) = \frac{1}{2} \mathrm{Tr} \, [\mathbf{C}_{,i} \mathbf{C}^{-1} \mathbf{C}_{,j} \mathbf{C}^{-1} \,], \tag{3}$$

where V_{sur} is the volume of the redshift survey, k denotes the amplitude of mode $\boldsymbol{k}$, μ is the cosine of the angle between mode $\boldsymbol{k}$ and the line of sight and $D(z)$ is the growth function at redshift z. $\mathbf{C}$ is the data matrix storing the observed galaxy power spectra P in redshift space,[8] and $\mathbf{C}_{,i}$ is the derivative matrix with respect to parameter p_i, As eBOSS target classes overlap, we shall explicitly show the Fisher matrix for the single- and multitracer cases in what follows.

3.1.1 The single-tracer case

If there is only one tracer being surveyed, which is the case for most of the sky covered by eBOSS,

$$C = P + \frac{1}{n}, \quad P = (b + f\mu^2)^2 P_{\mathrm{m}}(k), \tag{4}$$

---

[7] Note that this is the Fisher matrix using galaxies distributed in a given redshift slice. The final Fisher matrix is the sum over the Fisher matrices of individual redshift bins.

[8] We include the damping term in the power spectra to account for the Fingers-of-God (FoG) effect and for the redshift errors.

Table 2. Expected number of each target class in each redshift bin, and the volume density in units $10^{-4}\,h^3\,\mathrm{Mpc}^{-3}$ shown in parentheses. The effective redshift z_{eff}, total number of sources, observed surface area and galaxy bias of each target are shown in the last four rows.

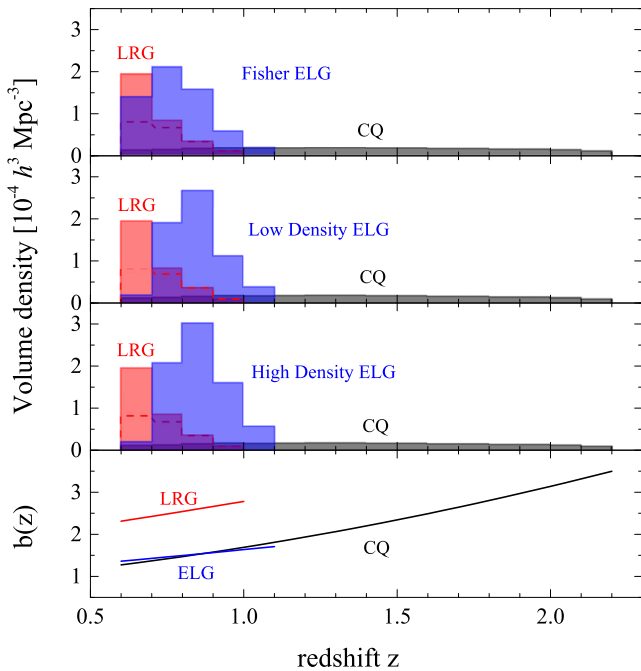| Redshift	CMASS LRGs	eBOSS LRGs	Clustering quasars	Fisher ELGs	Low-density DECam ELGs	High-density DECam ELGs
$0.6 < z < 0.7$	137 475 (1.137)	97 937 (0.810)	15 416 (0.119)	36 584 (1.412)	4425 (0.183)	3895 (0.205)
$0.7 < z < 0.8$	24 407 (0.170)	97 340 (0.678)	19 997 (0.130)	66 606 (2.165)	54 786 (1.908)	46 656 (2.068)
$0.8 < z < 0.9$	1645 (0.010)	57 600 (0.350)	27 154 (0.154)	58 328 (1.654)	87 979 (2.673)	78 462 (3.034)
$0.9 < z < 1.0$	183 (0.001)	17 815 (0.097)	33 649 (0.171)	24 557 (0.624)	41 690 (1.135)	46 321 (1.605)
$1.0 < z < 1.1$			35 056 (0.163)	9377 (0.218)	14 975 (0.373)	17 917 (0.568)
$1.1 < z < 1.2$			39 307 (0.170)	3736 (0.081)	6863 (0.159)	8173 (0.241)
$1.2 < z < 1.4$			87 984 (0.175)			
$1.4 < z < 1.6$			90 373 (0.166)			
$1.6 < z < 1.8$			86 631 (0.151)			
$1.8 < z < 2.0$			81 255 (0.137)			
$2.0 < z < 2.1$			36 760 (0.122)			
$2.1 < z < 2.2$			28 214 (0.093)			
z_{eff}	0.665	0.736	1.374	0.790	0.851	0.863
Total	163 710 (0.267)	270 692 (0.442)	581 796 (0.148)	199 188 (0.903)	210 718 (1.024)	201 424 (1.245)
Surface area	7000 deg^2	7000 deg^2	7500 deg^2	1500 deg^2	1400 deg^2	1100 deg^2
Bias	$1.7\frac{G(0)}{G(z)}$	$1.7\frac{G(0)}{G(z)}$	$0.53 + 0.29(1+z)^2$	$\frac{G(0)}{G(z)}$	$\frac{G(0)}{G(z)}$	$\frac{G(0)}{G(z)}$

Figure 1. The volume number density (in units of $10^{-4}\,h^3\,\mathrm{Mpc}^{-3}$) and galaxy bias of the LRGs (red), ELGs (blue) and clustering quasars (black). In the three upper panels, the red dashed lines show the eBOSS LRGs, and the red shaded region shows the eBOSS LRGs combined with the BOSS LRGs in the $z > 0.6$ tail.

where n, b, f, P_m denote the number density, bias, logarithmic growth rate and the matter power spectrum, respectively. In this case, equation (3) reduces to

$$\mathcal{F}_{ij}(k, \mu) = \frac{1}{2} D_i D_j R_V. \tag{5}$$

$$D_i = \frac{\partial \ln P}{\partial p_i}, \quad R_V \equiv \frac{V_{\mathrm{eff}}}{V_{\mathrm{sur}}} = \left(\frac{nP}{nP + 1}\right)^2, \tag{6}$$

where P, V_{eff} denote the power spectrum in redshift space and the effective volume, respectively.

3.1.2 The double-tracer case

If two tracers with different biases (denoted by A and B) are used to probe the same patch of the sky in the same redshift range, e.g. the eBOSS LRGs and ELGs, we need to include the cross-correlation, denoted by X, between them. In this case, **C** becomes a 2×2 matrix, namely,

$$\mathbf{C} = \begin{bmatrix} P_A + \frac{1}{n_A} & P_X \\ P_X & P_B + \frac{1}{n_B} \end{bmatrix}. \tag{7}$$

The Fisher matrix can be calculated by substituting **C** into equation (3), and we include an explicit calculation for the two-tracer case in Appendix A.

Compared to the single-tracer case, the auto- and cross-power spectra of multiple tracers provide measurements of ratios of f/b that couple radial and angular modes, beating radial sample variance in the low-noise limit (McDonald & Seljak 2009).

To illustrate the improvement of having multiple tracers, we show an example of the $f\sigma_8$ constraint using eBOSS LRGs and all the eBOSS tracers. We start by constraining $f\sigma_8$ using the eBOSS LRGs, and will show the improvement of the constraint when the ELGs and CQs are added to the analysis, with the cross-correlation included. The result is shown in Fig. 2, in which the ratio of the error on $f\sigma_8$ using multiple tracers to that using the eBOSS LRGs alone is plotted as a function of redshift.

As shown, the $f\sigma_8$ constraint will be improved when a full cross-correlation analysis among the ELGs, CQs and LRGs is possible in 2020. The improvement is maximal in the redshift bin of $0.9 < z < 1.0$, reducing the $f\sigma_8$ uncertainty from 13.7 to 5.4 per cent.

Note that this improvement is mainly due to the fact that more galaxies are available in the full cross-correlation analysis. Although the gain from the reduction of sample variance is subdominant for the case of eBOSS due to the level of shot noise, we show there will be a clear benefit from combining all of the available samples
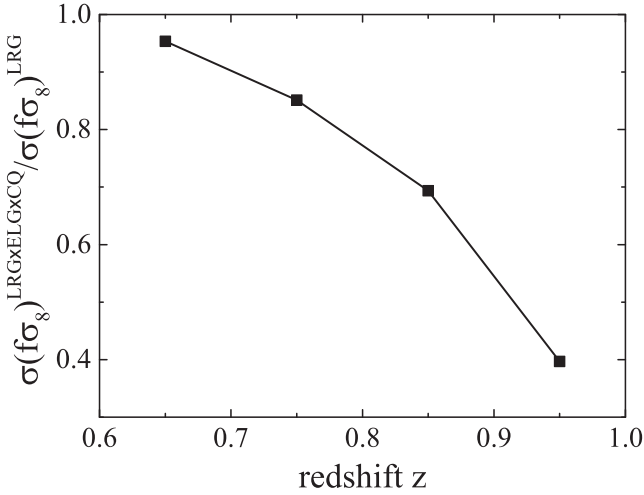
Figure 2. The ratio of the error of $f\sigma_8$ using all the eBOSS tracers to that using eBOSS LRGs alone.

and their cross-correlations. Further, we expect that using multiple tracers in the overlapping volume will be helpful to diagnose and reduce both observational and theoretical systematic uncertainties.

3.2 The Fisher matrix for the BAO of redshift surveys

To forecast the sensitivity of the BAO distance along and perpendicular to the line of sight for eBOSS, we follow Seo & Eisenstein (2007).

The two BAO parameters are

$$\ln(D_A/s), \ \ln(sH). \tag{8}$$

Note that

$$\sigma(\ln(D_A/s)) \simeq \ln D_A, \ \sigma(\ln(sH)) \simeq \ln H, \tag{9}$$

if the sound horizon s can be determined by external data such as the CMB, which can be achieved for eBOSS using *Planck* measurements (e.g. Planck Collaboration XIII 2015b).

3.3 The Fisher matrix for the RSD of redshift surveys

We follow White, Song & Percival (2009) to perform forecasts for the RSD parameters. The observable used is the full galaxy power spectrum in redshift space. To be consistent with the notation of White et al. (2009), we rewrite equation (4) as

$$P = \left[b\sigma_8(z) + f\sigma_8(z)\mu^2 \right]^2 \frac{P_m(k, z=0)}{\sigma_8^2(z=0)}, \tag{10}$$

i.e. for each redshift slice, we attach $\sigma_8(z)$ to $b(z)$ and $f(z)$ and use the products as parameters. Explicitly, the free parameters are

$$\ln[b\sigma_8(z)], \ \ln[f\sigma_8(z)]. \tag{11}$$

The derivatives of P with respect to these parameters are[9]

$$\frac{\partial \ln P}{\partial \ln(b\sigma_8)} = \frac{2b\sigma_8}{b\sigma_8 + f\sigma_8 \mu^2}, \tag{12}$$

$$\frac{\partial \ln P}{\partial \ln(f\sigma_8)} = \frac{2\mu^2 f\sigma_8}{b\sigma_8 + f\sigma_8 \mu^2}. \tag{13}$$

[9] We drop the dependence on z for brevity.

Note that, in the N-tracer case, p_1 needs to be extended into a set, namely,

$$p_1 = \{\ln(b_1\sigma_8), \ln(b_2\sigma_8), \ldots, \ln(b_N\sigma_8)\}. \tag{14}$$

3.4 The Fisher matrix for the primordial non-Gaussianity

In the context of the local ansatz for NG, where the Bardeen potential Φ contains a term that is quadratic in a Gaussian field ϕ, i.e. $\Phi = \phi + f_{NL}(\phi^2 - \langle\phi^2\rangle)$, a scale-dependent non-Gaussian bias $\Delta b(k)$ is induced (Dalal et al. 2008; Desjacques et al. 2009):

$$\Delta b(k) = 3 f_{NL}(b - p)\delta_c \frac{\Omega_m}{k^2 T(k)D(z)} \left(\frac{H_0}{c} \right)^2, \tag{15}$$

where p depends on the type of tracer (Slosar et al. 2008), δ_c is the critical linear overdensity for the collapse and $T(k)$ is the matter transfer function (normalized to unity on large scales).

The non-Gaussian bias is sensitive to any coupling between modes of very different scales, which could come from bispectra or higher order correlations in models other than the local ansatz. In that sense, the halo bias is an important probe of NG beyond the local ansatz. To constrain non-Gaussian models more generally, the non-Gaussian bias can be parametrized by

$$\Delta b(k) = 3 \mathcal{A}_{NL}(b - p)\delta_c \frac{\Omega_m}{k^2(k/k_p)^{\alpha-2} T(k)D(z)} \left(\frac{H_0}{c} \right)^2. \tag{16}$$

By allowing values of α different from 2, this form tests the scaling of the squeezed limit of the bispectrum. The coefficient $\mathcal{A}_{NL}$ may depend on the mass of the object (through the Gaussian bias) depending on the details of the bispectrum (Agarwal, Ho & Shandera 2014).

Applying the general Fisher matrix formalism presented in Section 3.1 to the forecast for f_{NL}, we simply use equation (1) but replace b with $b + \Delta b(k)$. In our analysis we set $p = 1$ for the LRGs and ELGs and $p = 1.6$ for the clustering quasars (Slosar et al. 2008). We report constraints for the standard local ansatz using $\delta_c = 1.686$. We also forecast constraints on α and $\mathcal{A}_{NL}$, expanding around their fiducial values.

Note that the multitracer method can provide large improvements on f_{NL} constraints (McDonald & Seljak 2009; Seljak 2009), as it measures bias ratios well, and these depend on f_{NL}.

3.5 The Fisher matrix for CMB and WL surveys

CMB and weak lensing (WL) surveys provide highly complementary cosmological information to galaxy redshift surveys. When eBOSS completes its mission in 2020, the full Dark Energy Survey (DES) data set will be available, in addition to the full *Planck* data (Planck Collaboration I 2015a). Therefore it makes sense to combine the predicted DES, *Planck* and eBOSS data sets for cosmological forecasts. In this subsection, we briefly describe the formalism, survey specifications and assumptions used to forecast for DES and *Planck* constraints.

We assume that the data product of WL experiments are the two-point angular power spectra C_ℓ, as is the case for the *Planck* survey. Then the Fisher matrix for parameters $\{p_i, p_j\}$ is (Tegmark et al. 1997)

$$F_{ij} = f_{sky} \sum_{\ell=\ell_{min}}^{\ell_{max}} \frac{2\ell+1}{2} \text{Tr} \left(\frac{\partial \mathbf{C}_\ell}{\partial p_i} \tilde{\mathbf{C}}_\ell^{-1} \frac{\partial \mathbf{C}_\ell}{\partial p_j} \tilde{\mathbf{C}}_\ell^{-1} \right), \tag{17}$$

where $\tilde{\mathbf{C}}_\ell$ is the observed data covariance matrix with elements $\tilde{C}_\ell^{XY}$ including noise:

$$\tilde{C}_\ell^{XY} = C_\ell^{XY} + N_\ell^{XY}. \tag{18}$$

The quantity f_{sky} is the fraction of sky being surveyed, and the minimum and maximum multipole ℓ_{min} and ℓ_{max} is set to be

$$\ell_{min} = \pi/(2 f_{sky}^{1/2}); \; \ell_{max} = k_{cut}\chi, \tag{19}$$

where χ is the comoving distance from $z = 0$ to the redshift slice in which the power spectra are measured, and we set $k_{cut} = 0.1$ Mpc^{-1} h to avoid using observables in the non-linear regime.

DES should ultimately comprise 5000 deg^2 of multiband, optical imaging probing the redshift range $0.1 < z < 1.3$ with a median redshift of $z_0 = 0.7$ and an approximate 1σ error of 0.05 in photometric redshift, i.e. $f_{sky} = 0.13$ and $\sigma(z) = 0.05(1 + z)$. We take the total galaxy number density distribution to be (Hu & Scranton 2004)

$$N_G(z) \propto z^2 \exp(-z/z_0)^2. \tag{20}$$

To resolve the radial mode, we subdivide the galaxies into multiple redshift slices and each slice is modelled as

$$N_{G_i}(z) = \frac{1}{2} N_G(z) \left[\mathrm{erfc}\left(\frac{z_{i-1} - z}{\sqrt{2}\sigma(z)}\right) - \mathrm{erfc}\left(\frac{z_i - z}{\sqrt{2}\sigma(z)}\right)\right], \tag{21}$$

where erfc is the complementary error function.

We use the WL shear power spectra of DES, and subdivide the total galaxies into four redshift slices. We model the noise power spectra to be

$$N_\ell^{\kappa_i\kappa_j} = \delta_{ij}\frac{\gamma_{rms}^2}{n_j}, \tag{22}$$

where γ_{rms} is the root mean square shear from the intrinsic ellipticity of the galaxies, and n_j is the total number in the jth redshift slice. We assume a projected angular density of galaxies $N_G = 10$ galaxies arcmin^{-2}, and $\gamma_{rms} = 0.18 + 0.042 z$ for DES. Cosmological forecasts using this specification of DES include Pogosian et al. (2005) and Zhao et al. (2009a,b).

We choose the sensitivity of the *Planck* satellite for the CMB forecast and use the temperature and polarization angular power spectra. The noise power spectra for the CMB are (Pogosian et al. 2005)

$$N_{\ell,c}^T = (\Delta_T \theta_{FWHM,c})^2 \exp\left[\frac{\ell(\ell + 1)\theta_{FWHM,c}^2}{8\ln2}\right],$$

$$N_{\ell,c}^P = (\Delta_P \theta_{FWHM,c})^2 \exp\left[\frac{\ell(\ell + 1)\theta_{FWHM,c}^2}{8\ln2}\right], \tag{23}$$

where T and P denote the 'temperature' and 'polarization', respectively, and $\theta_{FWHM,c}$ is the full width at half-maximum (FWHM) of the angular resolution for a given frequency channel c. The combined noise from all channels is then

$$N_\ell^T = \left[\sum_c \left(N_{\ell,c}^T\right)^{-1}\right]^{-1},$$

$$N_\ell^P = \left[\sum_c \left(N_{\ell,c}^P\right)^{-1}\right]^{-1}. \tag{24}$$

3.6 Parametrizations

The general parametrization we use is presented in Table 3, where we list the collection of all the parameters with their physical meaning, and the fiducial value used in the forecast. Note that, however, different subsets of this collection are used in different cases, as detailed in the rest of this subsection.

3.6.1 The parametrization for the BAO forecast

As described in Section 3.2 and listed as P_I of Table 3, the free parameters for the BAO forecast are $\ln(D_A/s)(z_i)$ and $\ln(sH)(z_i)$ in the redshift slice z_i. Thus for N_{zbin} slices, the total number of BAO parameters are $2N_{zbin}$.

Table 3. The parameters used in our forecast, their physical meaning and the fiducial values we choose, which are consistent with the *Planck* cosmology (Planck Collaboration XIII 2015b).

	Parameter	Meaning	Fiducial value
P_I	$\ln(D_A/s)(z_i)$	The transverse BAO distance for the ith redshift bin	The value for the fiducial cosmology
	$\ln(sH)(z_i)$	The line-of-sight BAO distance for the ith redshift bin	The value for the fiducial cosmology
P_{II}	$f(z_i)\sigma_8(z_i)$	The product of the logarithmic growth and σ_8 for the ith redshift bin	The value for the fiducial cosmology
	$b_A(z_i)\sigma_8(z_i)$	The product of the bias factor and σ_8 for the ith redshift bin	The value for the fiducial cosmology
	$\omega_b \equiv \Omega_b h^2$	The physical baryon energy density	0.022242
	$\omega_c \equiv \Omega_c h^2$	The physical dark matter energy density	0.11805
	H_0	The Hubble constant [km s^{-1} Mpc^{-1}]	68.14
P_{III}	τ	The optical depth	0.0949
	$\log[10^{10}A_s]$	The amplitude of the primordial power spectrum	3.098
	n_s	The spectral index of the primordial power spectrum	0.9675
	Σm_ν	The sum of the neutrino masses in the unit of eV	0.06
	w_0	The w_0 parameter in the CPL parametrization	-1
	w_a	The w_a parameter in the CPL parametrization	0
P_{IV}	w_i	The equation-of-state parameter of dark energy in the ith redshift bin	-1
	μ_{ij}	The effective Newton's constant in the $\{i, j\}$th pixel in the $\{k, z\}$ plane	1
	η_{ij}	The gravitational slip in the $\{i, j\}$th pixel in the $\{k, z\}$ plane	1
	f_{NL}	The non-Gaussianity parameter	0
	α	The power index for the general non-Gaussianity model	2

3.6.2 The parametrization for the RSD forecast

We follow the parametrization used in White et al. (2009), namely, for each redshift slice z_i, the free parameters for the RSD forecast are $\ln[f\sigma_8(z_i)]$ and $\ln[b\sigma_8(z_i)]$. Thus there are $2N_{zbin}$ RSD parameters for N_{zbin} slices in total. The RSD parameters are listed as P_{II} of Table 3 and described in Section 3.3.

3.6.3 The parametrization for the non-Gaussianity forecast

As described in Section 3.4, the free parameters for the NG forecast for the local model are f_{NL} and $b(z_i, T_j)$, where the indices i, j are for the redshift slices and the type of tracer, respectively. So for a redshift survey with N_T tracers and N_{zbin} redshift slices, the total number of parameters is $N_T \times N_{zbin} + 1$. We will also consider whether this data can constrain departures from the local ansatz, in which case we have an additional parameter, α.

3.6.4 The parametrization for the baseline cosmology

We use the six-parameter ΛCDM model, also dubbed the 'vanilla' model, as the baseline cosmology model. The parameters of this model are listed as P_{III} of Table 3.

3.6.5 The parametrization for the dark energy forecast

To forecast for the equation-of-state of dark energy, we adopt two different sets of parametrizations.

(i) The Chevallier–Polarski–Linder (CPL) parametrization (Chevallier & Polarski 2001; Linder 2003):

$$w(z) = w_0 + w_a \frac{z}{1+z}. \tag{25}$$

The free parameters are w_0, w_a with the vanilla parameters P_{III}.

(ii) Binned w: we discretise $w(z)$ into $M + 1$ piece-wise constant bins in z allowing the value of w in each bin to be an independent parameter. Since eBOSS will not be able to probe $z > 3$, we use M bins linearly separated in z for $0 \le z \le 3$ and a single bin for $z > 3$. This allows a principal component analysis (PCA) to be undertaken in Section 4.3.1. We take $M = 20$ and vary these parameters together with the baseline parameters.

3.6.6 The parametrization for the modified gravity forecast

We follow Zhao et al. (2009b) to take the most general parametrization for modified gravity. Working in the Newtonian gauge, the perturbed Friedmann–Robertson–Walker metric to the first order is

$$ds^2 = -a^2(\eta)[(1 + 2\Psi(\boldsymbol{x}, \eta))d\eta^2 - (1 - 2\Phi(\boldsymbol{x}, \eta))d\boldsymbol{x}^2],$$

where η is the conformal time and $a(\eta)$ the scale factor. In Fourier space, we write (Hu & Sawicki 2007; Bertschinger & Zukin 2008)

$$k^2\Psi = -\mu(k, a)4\pi Ga^2\rho\Delta,$$

$$\Phi/\Psi = \eta(k, a), \tag{26}$$

where Δ is the comoving matter density perturbation. The functions μ and η parametrize the MG effect: the function η describes anisotropic stresses, while μ quantifies a time- and scale-dependent rescaling of Newton's constant G. In ΛCDM, $\mu = \eta = 1$ since the anisotropic stress due to radiation is negligible in late times.

Similar to binning $w(z)$, we treat $\mu(k, z)$ and $\eta(k, z)$ as unknown functions and forecast how well we can constrain the eigenmodes

of them using PCA. Since they are two-variable functions in both k and a, we have to bin them in the (k, z) plane. We use the same $M + 1$ z-bins as w (see Section 3.6.5) and N k-bins ($0 \le z \le 30$, $10^{-5} \le k \le 0.2\,h\,Mpc^{-1}$), with each of the $(M + 1) \times N$ pixels having independent values of μ_{ij} and η_{ij}. We consider $w(z)$ as another unknown function with independent values in each of the $M + 1$ z-bins. We choose $M = N = 20$ and have checked that this binning is fine enough to ensure the convergence of the results. We use logarithmic k-bins on superhorizon scales and linear k-bins on subhorizon scales to optimize computational efficiency. As in Zhao et al. (2009a), we only consider information from scales well described by linear perturbation theory, which is only a fraction of the (k, z)-volume probed by future surveys. Since the evolution equations contain time derivatives of $\mu(k, z)$, $\eta(k, z)$ and $w(z)$, we follow Crittenden, Pogosian & Zhao (2009) and Zhao et al. (2009b) and use hyperbolic tangent functions to represent steps in these functions in the z-direction, while steps in the k-direction are left as step functions.

Similar to the PCA of $w(z)$, the pixilization of $\mu(k, z)$ and $\eta(k, z)$ is for the later 2D PCA, as detailed in Zhao et al. (2009b, 2015), Asaba et al. (2013) and Hall, Bonvin & Challinor (2013).

3.6.7 The parametrization for the neutrino mass forecast

To forecast for the neutrino mass constraint, we vary the sum of neutrino masses with the vanilla cosmological model parameters, i.e. $\sum m_\nu$ and the P_{III} parameters in Table 3, and take $\sum m_\nu = 0.06\,eV$ as the fiducial model.

4 RESULTS

In this section, we shall first present the expected precision of BAO and RSD measurements, and then the constraint on general cosmological parameters, including the NG, dark energy and modified gravity parameters and the neutrino mass.

4.1 The BAO and RSD forecast

The primary BAO and RSD forecasts are shown in Tables 4 and 5 and in Figs 3 and 4. Table 4 lists the predicted 68 per cent CL fractional uncertainty on the BAO and RSD parameters, including the angular diameter distance $D_A(z)$, the Hubble parameter $H(z)$, the combined distance $D_V \equiv [cz(1 + z)^2 D_A(z)^2 H^{-1}(z)]^{1/3}$, $f(z)\sigma_8(z)$ and $b(z)\sigma_8(z)$ using various tracers in multiple redshift slices. For each tracer, we also list the forecast result at the effective redshift, and we find that eBOSS LRGs ($0.6 < z < 1.0$, combined with the BOSS LRGs at $z > 0.6$), ELGs ($0.6 < z < 1.2$) and CQs ($0.6 < z < 2.2$) can achieve the 1.0, 2.3 and 1.6 per cent precision, respectively, for the D_V measurement. Using the same samples, the constraint on $f\sigma_8$ is expected to be 2.5, 3.4 and 2.8 per cent, respectively.

Fig. 3 shows the forecasted BAO distance using eBOSS LRGs, in comparison with the BOSS measurement. The solid curves show the ΛCDM prediction, and the upper and lower limits of the bands correspond to the CPL model with $w_0 = -1.5$, $w_a = 1.0$ and $w_0 = -0.5$, $w_a = -1$, respectively. As shown, the eBOSS LRGs sample effectively extends the redshift range of BOSS to higher redshifts with a comparable precision on the distance measurement, namely, 1 per cent sensitivity on D_V over $0.6 < z < 1.0$.

Table 5 shows the constraint on $f\sigma_8$ using the three different combined eBOSS samples, depending on the ELGs target selection option, namely, Combined I: LRGs+Fisher ELGs+CQs; Combined

Table 4. The predicted 68 per cent CL error of the BAO distances and RSD parameters using various tracers in different redshift slices. In the last row for each tracer, we show the forecast using the total of all targets distributed across all redshift slices. We also show the effective redshift in parentheses.

Sample	Redshift	$\bar{n}P_{0.2,0}$	σ_{D_A}/D_A	σ_H/H	σ_{D_V}/D_V	$\sigma_{f\sigma_8}/f\sigma_8$	$\sigma_{b\sigma_8}/b\sigma_8$
	$0.6 < z < 0.7$	0.684	0.030	0.049	0.020	0.048	0.007
	$0.7 < z < 0.8$	0.102	0.073	0.106	0.047	0.104	0.016
CMASS LRGs	$0.8 < z < 0.9$	0.006	0.830	1.109	0.523	1.083	0.173
	$0.9 < z < 1.0$	0.0006	7.439	9.955	4.690	9.936	1.557
	$0.6 < z < 1.0$ ($z_{\rm eff} = 0.665$)	0.161	0.027	0.040	0.017	0.039	0.006
	$0.6 < z < 0.7$	0.487	0.034	0.054	0.022	0.053	0.008
	$0.7 < z < 0.8$	0.408	0.032	0.050	0.021	0.051	0.007
eBOSS LRGs	$0.8 < z < 0.9$	0.211	0.041	0.062	0.026	0.063	0.009
	$0.9 < z < 1.0$	0.058	0.094	0.134	0.060	0.137	0.021
	$0.6 < z < 1.0$ ($z_{\rm eff} = 0.736$)	0.266	0.019	0.030	0.013	0.029	0.004
	$0.6 < z < 0.7$	1.172	0.026	0.043	0.017	0.043	0.006
	$0.7 < z < 0.8$	0.510	0.029	0.046	0.019	0.047	0.007
CMASS+eBOSS LRGs	$0.8 < z < 0.9$	0.217	0.040	0.061	0.026	0.062	0.009
	$0.9 < z < 1.0$	0.059	0.093	0.133	0.059	0.136	0.020
	$0.6 < z < 1.0$ ($z_{\rm eff} = 0.707$)	0.427	0.016	0.025	0.010	0.025	0.004
	$0.6 < z < 0.7$	0.294	0.090	0.130	0.058	0.085	0.021
	$0.7 < z < 0.8$	0.451	0.065	0.097	0.042	0.065	0.015
	$0.8 < z < 0.9$	0.344	0.064	0.094	0.041	0.064	0.015
Fisher ELGs	$0.9 < z < 1.0$	0.130	0.105	0.140	0.066	0.098	0.024
	$1.0 < z < 1.1$	0.045	0.222	0.275	0.137	0.196	0.050
	$1.1 < z < 1.2$	0.017	0.514	0.611	0.316	0.444	0.115
	$0.6 < z < 1.2$ ($z_{\rm eff} = 0.790$)	0.188	0.037	0.051	0.023	0.034	0.009
	$0.6 < z < 0.7$	0.381	0.038	0.458	0.238	0.299	0.084
	$0.7 < z < 0.8$	0.397	0.071	0.105	0.045	0.070	0.017
	$0.8 < z < 0.9$	0.557	0.054	0.082	0.035	0.056	0.013
Low-density ELGs	$0.9 < z < 1.0$	0.236	0.074	0.104	0.047	0.073	0.018
	$1.0 < z < 1.1$	0.078	0.149	0.191	0.093	0.137	0.034
	$1.1 < z < 1.2$	0.033	0.286	0.351	0.177	0.256	0.065
	$0.6 < z < 1.2$ ($z_{\rm eff} = 0.851$)	0.213	0.035	0.048	0.022	0.033	0.008
	$0.6 < z < 0.7$	0.043	0.397	0.473	0.244	0.309	0.087
	$0.7 < z < 0.8$	0.431	0.077	0.115	0.050	0.077	0.018
	$0.8 < z < 0.9$	0.632	0.058	0.090	0.038	0.061	0.014
High-density ELGs	$0.9 < z < 1.0$	0.334	0.069	0.101	0.044	0.071	0.017
	$1.0 < z < 1.1$	0.118	0.122	0.162	0.077	0.117	0.029
	$1.1 < z < 1.2$	0.050	0.225	0.282	0.140	0.207	0.052
	$0.6 < z < 1.2$ ($z_{\rm eff} = 0.863$)	0.259	0.035	0.050	0.022	0.034	0.008
	$0.6 < z < 0.7$	0.022	0.267	0.300	0.163	0.189	0.058
	$0.7 < z < 0.8$	0.025	0.211	0.243	0.129	0.158	0.046
	$0.8 < z < 0.9$	0.032	0.158	0.187	0.097	0.126	0.035
	$0.9 < z < 1.0$	0.037	0.127	0.155	0.079	0.109	0.028
	$1.0 < z < 1.1$	0.037	0.120	0.148	0.074	0.109	0.027
	$1.1 < z < 1.2$	0.041	0.104	0.132	0.065	0.101	0.024
Clustering quasars	$1.2 < z < 1.4$	0.045	0.063	0.082	0.039	0.067	0.014
	$1.4 < z < 1.6$	0.047	0.057	0.076	0.036	0.068	0.013
	$1.6 < z < 1.8$	0.047	0.054	0.075	0.034	0.072	0.012
	$1.8 < z < 2.0$	0.047	0.052	0.074	0.033	0.078	0.012
	$2.0 < z < 2.1$	0.045	0.076	0.108	0.049	0.121	0.017
	$2.1 < z < 2.2$	0.036	0.092	0.132	0.059	0.153	0.021
	$0.6 < z < 2.2$ ($z_{\rm eff} = 1.374$)	0.040	0.025	0.033	0.016	0.028	0.006

II: LRGs+low-density ELGs+CQs; Combined III: LRGs+high-density ELGs+CQs. The cross-correlation of the power spectra is included in the overlapping region of different tracers.

Fig. 4 shows the fractional constraint on D_A, H and $f\sigma_8$ for individual tracers and for the three combined samples. From this figure, we can tell that the following.

(i) The CMASS LRGs sample at $z > 0.6$ is very helpful for both distance and RSD measurements at $0.6 < z < 0.7$, e.g. it improves the eBOSS LRGs constraint on D_A from 3.4 to 2.6 per cent, and improves the $f\sigma_8$ constraint from 5.3 to 4.3 per cent.

(ii) The constraints from the ELGs samples are generally weaker than those using the LRGs samples, namely, the uncertainty is

Table 5. Predictions for the precision of $f\sigma_8$ measurements obtained using the multitracer technique, using three different eBOSS data combinations: I: LRGs+Fisher ELG+clustering quasar; II: LRGs+low-density ELG+clustering quasar; III: LRGs+high-density ELG+clustering quasar.

Sample	Redshift range	$\sigma_{f\sigma_8}/f\sigma_8$
	$0.6 < z < 0.7$	0.039
	$0.7 < z < 0.8$	0.039
	$0.8 < z < 0.9$	0.043
	$0.9 < z < 1.0$	0.061
	$1.0 < z < 1.1$	0.088
	$1.1 < z < 1.2$	0.094
Combined I	$1.2 < z < 1.4$	0.067
	$1.4 < z < 1.6$	0.068
	$1.6 < z < 1.8$	0.072
	$1.8 < z < 2.0$	0.078
	$2.0 < z < 2.1$	0.121
	$2.1 < z < 2.2$	0.153
	$0.6 < z < 0.7$	0.041
	$0.7 < z < 0.8$	0.040
	$0.8 < z < 0.9$	0.041
	$0.9 < z < 1.0$	0.054
	$1.0 < z < 1.1$	0.080
	$1.1 < z < 1.2$	0.088
Combined II	$1.2 < z < 1.4$	0.067
	$1.4 < z < 1.6$	0.068
	$1.6 < z < 1.8$	0.072
	$1.8 < z < 2.0$	0.078
	$2.0 < z < 2.1$	0.121
	$2.1 < z < 2.2$	0.153
	$0.6 < z < 0.7$	0.041
	$0.7 < z < 0.8$	0.040
	$0.8 < z < 0.9$	0.043
	$0.9 < z < 1.0$	0.054
	$1.0 < z < 1.1$	0.076
	$1.1 < z < 1.2$	0.086
Combined III	$1.2 < z < 1.4$	0.067
	$1.4 < z < 1.6$	0.068
	$1.6 < z < 1.8$	0.072
	$1.8 < z < 2.0$	0.078
	$2.0 < z < 2.1$	0.121
	$2.1 < z < 2.2$	0.153

roughly larger by a factor of 2, and 1.4 for the distance and RSD measurement, respectively.

(iii) We find that the three different ELGs target selection options yield similar results, especially when combined with LRGs and CQ. The high-density selection option has the highest $z_{\rm eff}$, being 0.863. Thus in the following cosmological forecasts, we choose to use this option for the ELGs to form a combined eBOSS sample, dubbed 'Combined III'.

(iv) For the distance measurement using the combined eBOSS sample (Combined III), we expect to have 1, 2 and 1.6 per cent sensitivity on D_V at the effective redshifts of 0.71, 0.86 and 1.37 using the LRGs, ELGs and CQs samples, respectively.

(v) For the $f\sigma_8$ measurement, the LRGs, ELGs and CQs provide a 2.5, 3.4 and 2.8 per cent precision at the effective redshifts of 0.71, 0.86 and 1.37, respectively. Considering narrow slices, the combined sample will allow between 4 and 15 per cent precision to be obtained in redshift slices that are between 0.1 and 0.2 thick (see Table 5 for details).

Fig. 5 shows the predicted $f\sigma_8$ measurement errors using the combined eBOSS samples, together with the theoretical predictions
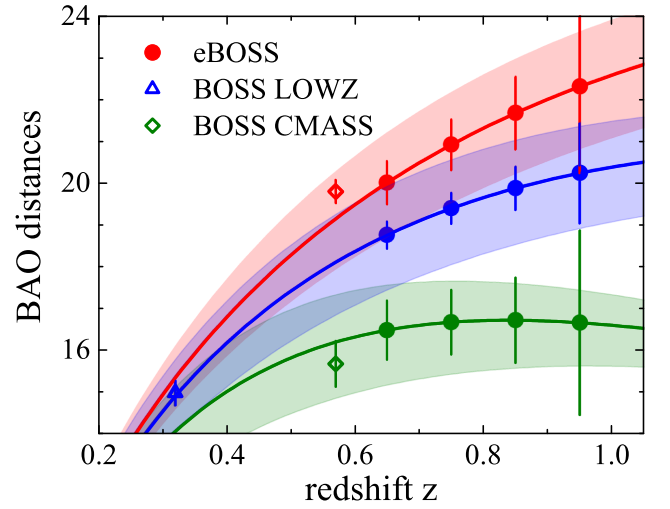

Figure 3. The BAO distance measurement using the eBOSS LRGs, in comparison with that using the BOSS LOWZ and CMASS samples. The top red, middle blue and bottom green data and error bands show $(1 + z)D_{\rm A}(z)/r_{\rm d}\sqrt{z}$, $D_V(z)/(r_{\rm d}\sqrt{z})$ and $c\sqrt{z}/[H(z)r_{\rm d}]$, respectively. The $\sqrt{z}$ factor is included to tune the dynamical ranges for the purpose of visualization.
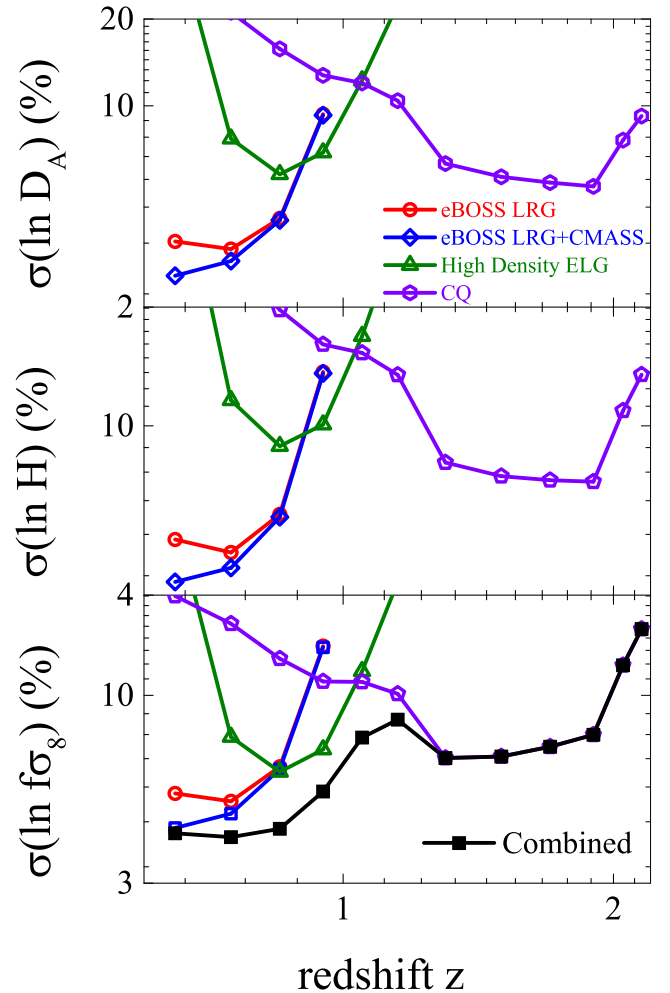

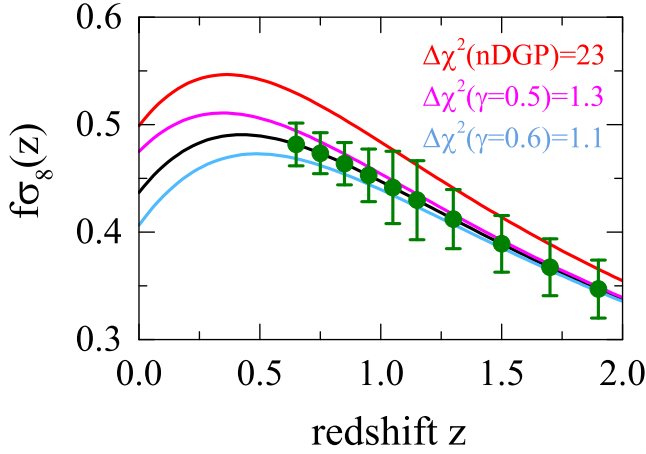**Figure 4.** The BAO and RSD constraint using various eBOSS tracers.

Figure 5. The predicted constraint on $f\sigma_8$ as a function of redshift using combinations of three eBOSS tracers. All models have the same background expansion, giving the same comoving BAO position. The black curve shows the growth in a ΛCDM Universe, assuming the *Planck* best-fitting model parameters. The red curve shows the nDGP model (Dvali, Gabadadze & Porrati 2000) with $\Omega_{r_c} = 0.17$, which corresponds to $r_c H_0 = 1.2$, and $\sigma_8 = 0.90$. The magenta and blue curves show two phenomenological modified gravity models with $\gamma = 0.5$ and 0.6, respectively, where $f(z) = \Omega_M(z)^\gamma$ (Linder 2005).

Table 6. Forecasted results of f_{NL} using different tracers individually and three combinations of eBOSS data, depending on the target selection plan for the ELG. The results with and without marginalization over the bias factor are shown.

Sample	Redshift	$\sigma(f_{NL})$ (Bias float)	$\sigma(f_{NL})$ (Bias fixed)
CMASS LRGs	$0.6 < z < 1.0$	37.99	24.22
eBOSS LRGs	$0.6 < z < 1.0$	23.73	15.62
CMASS+eBOSS LRGs	$0.6 < z < 1.0$	22.63	14.52
Fisher ELGs	$0.6 < z < 1.2$	94.75	56.94
Low-density ELGs	$0.6 < z < 1.2$	87.98	52.41
High-density ELGs	$0.6 < z < 1.2$	92.61	53.78
Clustering quasars	$0.6 < z < 2.2$	20.56	15.74
Combined I	$0.6 < z < 2.2$	15.03	10.50
Combined II	$0.6 < z < 2.2$	15.01	10.47
Combined III	$0.6 < z < 2.2$	15.03	10.48

for the ΛCDM, nDGP with $r_c H_0 = 1.2$, and two phenomenological MG models parametrized by the growth index γ, i.e. $f(z) = \Omega(z)^\gamma$ (Linder 2005). The models with $\gamma = 0.5$ and 0.6 are shown. As shown, eBOSS alone can distinguish the $\gamma = 0.5$ and 0.6 models from the ΛCDM model, and can rule out the nDGP model at a significance of 4.8σ.

4.2 Primordial non-Gaussianity

The forecast result for f_{NL} (the local ansatz) is given in Table 6, where we show the 68 per cent CL predicted error on f_{NL} using different tracers individually and three combinations of eBOSS data, depending on the target selection plan for the ELG. As shown

$$\sigma(f_{NL}) \sim 15 \text{ (bias float)}; \ \sigma(f_{NL}) \sim 10.5 \text{ (bias fixed)}. \quad (27)$$

In addition, we consider the more general parametrization given in equation (16). Since the data are insufficient to constrain the scale dependence of the non-Gaussian bias as a free parameter, we choose fiducial values for α and report constraints on the amplitude

and scale dependence. For example, choosing $\mathcal{A}_{NL} = 5$ at a pivot scale of $k = 0.1\,\mathrm{Mpc}^{-1}$ (and fixing the Gaussian bias of all tracers), the Combined I data set yields $\sigma(\mathcal{A}_{NL}) = 18$ and $\sigma(\alpha) = 2.6$ at 65 per cent CL. This result is not very constraining, but it will be interesting to combine the eventual eBOSS LRGs sample with the full BOSS sample (see the results in Agarwal et al. 2014) to obtain a tighter constraint.

4.3 Other cosmological parameters

In this subsection, we make predictions of how sensitive the full eBOSS galaxy power spectrum will be to cosmological parameters, when combined with external data sets including CMB and WL. We form an eBOSS data set by combining the LRGs (with the BOSS LRGs at $z > 0.6$), high-density ELGs, clustering quasars with all the cross-correlations included. We also include BAO measurements at $z \sim 2.4$ using Lyα forest from BOSS (Busca et al. 2013; Font-Ribera et al. 2014; Delubac et al. 2015) and eBOSS (Dawson et al. 2015), at 2 and 1.2 per cent precision, respectively.[10] We refer to this combined data as 'eBOSS' in the following forecasts, unless specifically mentioned otherwise. We use MGCAMB (Zhao et al. 2009a; Hojjati, Pogosian & Zhao 2011),[11] which is a modified version of CAMB (Lewis, Challinor & Lasenby 2000) to calculate the observables and use COSMOFISH[12] for the Fisher matrix calculation. We include the dark energy perturbation following the prescription in Zhao et al. (2005).

4.3.1 Dark energy EoS

The result for the CPL parametrization is presented in Fig. 6, where the 68 and 95 per cent CL contour plots of $\{w_0, w_a\}$ are shown. The grey and blue contours illustrate the result for BOSS and BOSS+eBOSS, respectively,[13] combined with the full *Planck* data and the H_0 measurement, and the left- and right-hand panels show the prediction without and with the Lyα forest data combined. As shown in the legend, the FoM, which is inversely proportional to the area of the contours, can be improved by a factor of 3.0 (2.2) when the eBOSS data is combined with (without) the Lyα forest. The Lyα forest, which provides BAO measurement at high redshift, is highly complementary to the BAO measurement using BOSS/eBOSS galaxies at lower redshifts since the former can help to break the degeneracy between dark energy parameters and Ω_M, and the latter provides more direct constraint since dark energy dominates at low redshifts, i.e. $z \lesssim 1$.

The factor of 3 improvement on the FoM motivated us to explore more details of $w(z)$ using eBOSS by going beyond the CPL parametrization. As described in (II) of Section 3.6.5, we forecast the binned $w(z)$, obtained the Fisher matrix of the w bins $\mathbf{F}_w$ with all other cosmological parameters marginalized over, and perform a PCA on $\mathbf{F}_w$ to determine the eigenmodes that can be well constrained, i.e.

$$\mathbf{F}_w = \mathbf{W}^\mathrm{T} \Lambda \mathbf{W}, \quad (28)$$

---

[10] There are other possibilities to measure the BAO signal using the triply ionized carbon (C IV) as a tracer in the eBOSS survey, as discussed in Pieri (2014).

[11] Available at http://icosmology.info/MGCAMB.html

[12] For more information about the COSMOFISH package, check http://icosmology.info/cosmofish.html

[13] When combining BOSS with eBOSS galaxies, we take BOSS galaxies in the redshift range of $z < 0.6$ to avoid double counting.
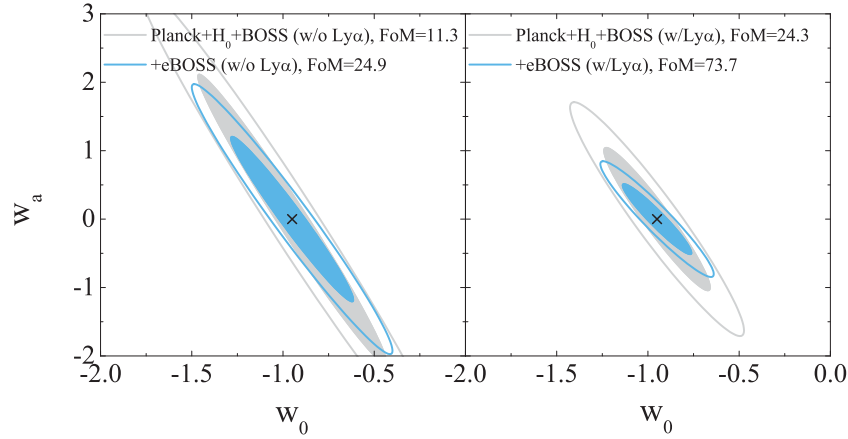
Figure 6. Current constraints on the DETF model for time-varying dark energy compared to projected constraints from eBOSS. We report constraints from the BAO probes, *Planck*, and H_0 from *HST* observations of SNe Ia. For all measurements, the filled ellipse represents the 68 per cent confidence interval and the open ellipse represents the 95 per cent confidence interval.

where the *i*th rows of the decomposition matrix **W**, $e_i(z)$ is the *i*th eigenvector of $w(z)$ and the (i, i) element of the diagonal matrix **Λ** stores the corresponding eigenvalue, λ_i. This enables an orthonormal decomposition of arbitrary $w(z)$, i.e.

$$1 + w(z) = \sum_{i=1}^{N} \alpha_i e_i(z), \ \lambda_i = \sigma(\alpha_i)^{-2}. \tag{29}$$

We refer the readers to Huterer & Starkman (2003) and Crittenden et al. (2009, 2012) for more details of PCA for $w(z)$.

Fig. 7 shows the PCA result using *Planck*, *Planck*+DES, *Planck*+DES+eBOSS data, respectively. As shown, the uncertainty of the best constrained eigenmode using eBOSS data (combined with *Planck* and DES) is ∼0.05, and there are three modes which can be measured with uncertainty below 0.5.

4.3.2 Modified gravity

As described in Section 3.6.6, we bin the functions $\mu(k, z)$ and $\eta(k, z)$, and obtain a Fisher matrix for all the bins with all other cosmological parameters marginalized over. Then as for the PCA procedure used for $w(z)$, we perform a PCA on the μ and η functions (we marginalize over all the η bins when performing the PCA on μ and vice versa).

It is clear from equation (26) that μ determines the growth of structure via the modified Poisson equation, so it can be constrained by redshift surveys like eBOSS. On the other hand, η affects the lensing potential thus it could be probed by the CMB and WL surveys instead. Since the purpose of this paper is to highlight the cosmological potential of eBOSS, we show the PCA result of μ only in Fig. 8. eBOSS significantly augments the *Planck*+DES constraint on the μ modes. The uncertainty on the best-constrained mode is reduced by a factor of 10, and eBOSS helps to constrain five modes to a precision better than 10 per cent.

4.4 Neutrino mass

The total neutrino mass as a function of the mass of the lightest species is plotted in Fig. 9 to illustrate the normal and inverted mass hierarchy, which are degenerate at the high-mass end but in principle distinguishable at the low-mass end by cosmological probes.
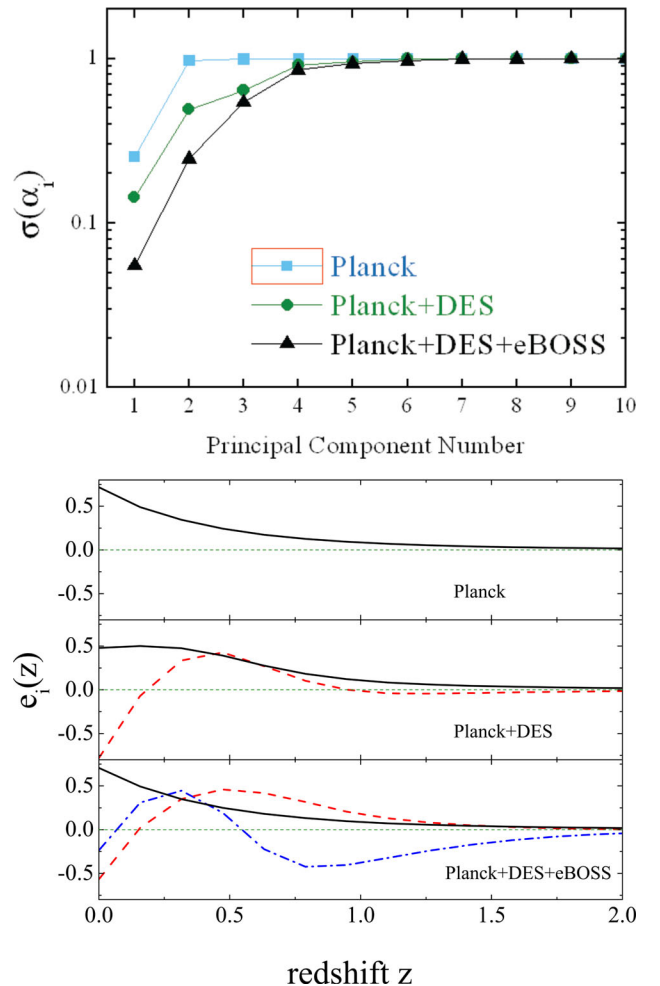

Figure 7. Upper: the forecasted 68 per cent CL measurement error on α_i, the coefficient of the *i*th principal components of $w(z) + 1$, namely, $w(z) + 1 = \sum_i \alpha_i e_i(z)$, using different data combinations illustrated in the legend. A weak prior of $\sigma(w(z)) < 1$ was assumed. Lower: the best determined eigenvectors (with errors less than 0.5) of $w(z)$ for different data combinations shown in the legends. The modes are shown, in the order from better constrained to worse, as black solid, red dashed, blue dash–dot, purple dash–dot–dot and brown short dash–dot curves. The short dashed green horizon line shows $e_i(z) = 0$.
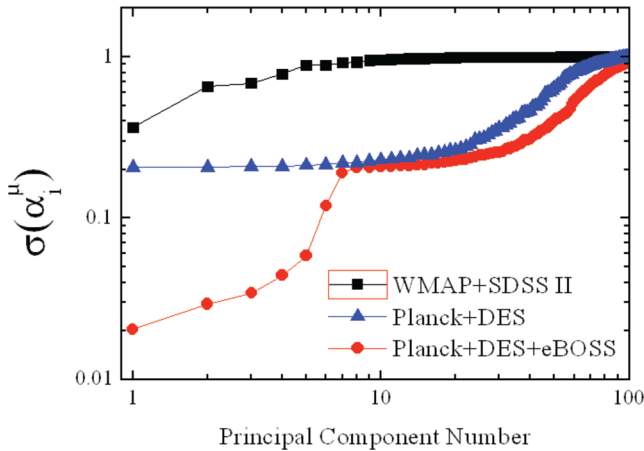
Figure 8. The forecasted 68 per cent CL error on the coefficients of the principal components of $\mu(k, z)$ for different data combinations shown in the legend.
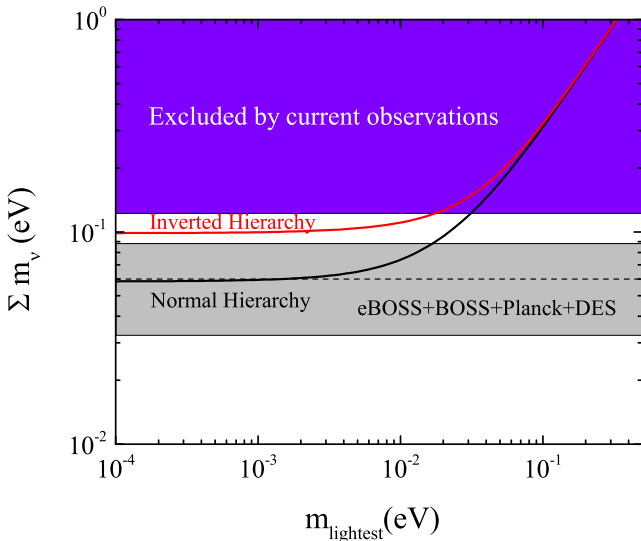

Figure 9. The neutrino mass constraint. The purple shaded region is excluded by the current observations, and the grey shaded band is the expected 68 per cent CL uncertainty using the full eBOSS survey combined with BOSS, DES and *Planck*. The black and red curves illustrate the theoretical prediction for the normal and inverted neutrino mass hierarchies.

BOSS, combined with other current surveys, has put an upper limit on the neutrino mass of $\sum m_\nu < 0.12$ eV (95 per cent CL; Palanque-Delabrouille et al. 2015a,b), which is shown by the purple shaded region in Fig. 9. This is not enough to distinguish between NH and IH. Assuming the fiducial value of the total neutrino mass to be 0.06 eV and using eBOSS combined with BOSS, DES and *Planck*, we predict the error on the neutrino mass to be

$$\sigma\left(\Sigma m_\nu\right) = 0.03\,\mathrm{eV}. \tag{30}$$

This is sufficient to break the degeneracy between the NH and IH scenarios, as shown in Fig. 9, e.g. a measurement of $\sigma(\Sigma m_\nu) < 0.06 \pm 0.03$ would rule out the IH at 1σ level.

5 CONCLUSIONS AND DISCUSSIONS

As the successor of the BOSS survey, the eBOSS survey of the SDSS-IV project is the largest current spectroscopic survey in the world. eBOSS will map the Universe in the redshift range $0.6 < z < 2.2$ using multiple tracers and thereby improve our knowledge of the nature of dark energy, test models of gravity, constrain the initial conditions of the Universe and measure the sum of the mass of neutrinos.

In this work, we have investigated the ability of the eBOSS survey to make BAO distance and RSD growth rate measurements, and explored the potential of eBOSS for the studies of dark energy, modified gravity, the primordial NG and the neutrino mass.

We find that eBOSS will provide strong BAO and RSD measurements in the redshift range of $0.6 < z < 2.2$ using tracers of the LRGs, ELGs and CQs, namely, the eBOSS LRGs (combined with the BOSS LRGs at $z > 0.6$), ELGs and CQs will reach 1, 2 and 1.6 per cent sensitivity on the BAO distance D_V measurement at effective redshifts of 0.71, 0.86 and 1.37, respectively. The RSD effect quantified by $f\sigma_8$, will be measured at a sensitivity of 2.5, 3.4 and 2.8 per cent by these tracers at the same effective redshifts, respectively. The recent work of Zhu, Padmanabhan & White (2015) provides a promising approach to optimize distance–redshift measurements in the BAO. Introducing a small number of redshift weights are demonstrated on a toy model to preserve nearly all of the BAO information at different redshifts. Such an optimization will be particularly effective for surveys like eBOSS which spans a wide range of redshift. A similar z-weighting technique is also likely to be efficient in improving growth rate measurements from the RSD signal (Ruggeri et al., in preparation; Zhao et al., in preparation).

The exquisite BAO and RSD measurements that eBOSS will provide are key for dark energy and gravity studies. Choosing a CPL parametrization for the EoS of dark energy, eBOSS can improve the FoM of dark energy by a factor of 3, with respect to the current BOSS measurement. A more general PCA study of $w(z)$ reveals that eBOSS, combined with DES and *Planck*, will be able to measure three eigenmodes of $w(z)$ with 5 per cent precision. For modified gravity, a general PCA study finds that eBOSS can significantly improve the constraint on the eigenmodes of μ, the effective Newton's constant, enhancing the DES+*Planck* constraint. Specifically, eBOSS can improve the constraint on the best-determined mode by a factor of 10, and make it possible to measure five modes better than the 10 per cent accuracy.

We find that eBOSS alone can determine f_{NL}, the parameter quantifying primordial NG, to a precision of $\sigma(f_{\mathrm{NL}}) = 10$ in the optimistic case in which the bias can be well determined separately. When combined with DES and *Planck*, eBOSS can weigh neutrinos to a precision of $\sigma(\sum m_\nu) = 0.03$ eV, which makes it possible to determine the neutrino mass hierarchy.

REFERENCES

Agarwal N., Ho S., Shandera S., 2014, J. Cosmol. Astropart. Phys., 2, 38
Albrecht A. et al., 2009, preprint (arXiv:0901.0721)
Anderson L. et al., 2014, MNRAS, 441, 24
Asaba S., Hikage C., Koyama K., Zhao G.-B., Hojjati A., Pogosian L., 2013, J. Cosmol. Astropart. Phys., 8, 29
Bertschinger E., Zukin P., 2008, Phys. Rev. D, 78, 024015
Beutler F. et al., 2014, MNRAS, 444, 3501
Bolton A. S. et al., 2012, AJ, 144, 144
Bovy J. et al., 2012, ApJ, 749, 41
Busca N. G. et al., 2013, A&A, 552, A96
Chevallier M., Polarski D., 2001, Int. J. Modern Phys. D, 10, 213
Clifton T., Ferreira P. G., Padilla A., Skordis C., 2012, Phys. Rep., 513, 1
Crittenden R. G., Pogosian L., Zhao G.-B., 2009, J. Cosmol. Astropart. Phys., 12, 25
Crittenden R. G., Zhao G.-B., Pogosian L., Samushia L., Zhang X., 2012, J. Cosmol. Astropart. Phys., 2, 48
Croom S. M. et al., 2005, MNRAS, 356, 415
Dalal N., Doré O., Huterer D., Shirokov A., 2008, Phys. Rev. D, 77, 123514
Dawson K. S. et al., 2013, AJ, 145, 10
Dawson K. S. et al., 2015, AJ, in press (arXiv:1508.04473)
Delubac T. et al., 2015, A&A, 574, A59
Desjacques V., Seljak U., Iliev I. T., 2009, MNRAS, 396, 85
Dolgov A. D., 2002, Phys. Rep., 370, 333
Dvali G., Gabadadze G., Porrati M., 2000, Phys. Lett. B, 485, 208
Eisenstein D. J. et al., 2011, AJ, 142, 72
Flaugher B. et al., 2015, AJ, 150, 150
Font-Ribera A. et al., 2014, J. Cosmol. Astropart. Phys., 5, 27
Fukugita M., Ichikawa T., Gunn J. E., Doi M., Shimasaku K., Schneider D. P., 1996, AJ, 111, 1748
Gunn J. E. et al., 2006, AJ, 131, 2332
Hall A., Bonvin C., Challinor A., 2013, Phys. Rev. D, 87, 064026
Hojjati A., Pogosian L., Zhao G.-B., 2011, J. Cosmol. Astropart. Phys., 8, 5
Hu W., Sawicki I., 2007, Phys. Rev. D, 76, 104043
Hu W., Scranton R., 2004, Phys. Rev. D, 70, 123002
Huterer D., Starkman G., 2003, Phys. Rev. Lett., 90, 031101
Kaiser N., 1987, MNRAS, 227, 1
Lesgourgues J., Pastor S., 2006, Phys. Rep., 429, 307

Lewis A., Challinor A., Lasenby A., 2000, ApJ, 538, 473
Linder E. V., 2003, Phys. Rev. Lett., 90, 091301
Linder E. V., 2005, Phys. Rev. D, 72, 043529
McDonald P., Seljak U., 2009, J. Cosmol. Astropart. Phys., 10, 7
Myers A. D. et al., 2015, ApJS, 221, 27
Olive K., Particle Data Group, 2014, Chin. Phys. C, 38, 090001
Palanque-Delabrouille N. et al., 2015a, J. Cosmol. Astropart. Phys., 2, 45
Palanque-Delabrouille N. et al., 2015b, J. Cosmol. Astropart. Phys., 11, 011
Perlmutter S. et al., 1999, ApJ, 517, 565
Pieri M. M., 2014, MNRAS, 445, L104
Planck Collaboration I, 2015a, preprint (arXiv:1502.01582)
Planck Collaboration XIII, 2015b, preprint (arXiv:1502.01589)
Pogosian L., Corasaniti P. S., Stephan-Otto C., Crittenden R., Nichol R., 2005, Phys. Rev. D, 72, 103519
Prakash A. et al., 2015, ApJS, submitted (arXiv:1508.04478)
Raichoor A. et al., 2016, A&A, 585, A50
Riess A. G. et al., 1998, AJ, 116, 1009
Ross N. P. et al., 2009, ApJ, 697, 1634
Ross A. J. et al., 2013, MNRAS, 428, 1116
Rossi G., Yèche C., Palanque-Delabrouille N., Lesgourgues J., 2015, Phys. Rev. D, 92, 063505
Samushia L. et al., 2014, MNRAS, 439, 3504
Seljak U., 2009, Phys. Rev. Lett., 102, 021302
Seo H.-J., Eisenstein D. J., 2007, ApJ, 665, 14
Slosar A., Hirata C., Seljak U., Ho S., Padmanabhan N., 2008, J. Cosmol. Astropart. Phys., 8, 31
Smee S. A. et al., 2013, AJ, 146, 32
Tegmark M., 1997, Phys. Rev. Lett., 79, 3806
Tegmark M., Taylor A. N., Heavens A. F., 1997, ApJ, 480, 22
Weinberg D. H., Mortonson M. J., Eisenstein D. J., Hirata C., Riess A. G., Rozo E., 2013, Phys. Rep., 530, 87
White M., Song Y.-S., Percival W. J., 2009, MNRAS, 397, 1348
Wright E. L. et al., 2010, AJ, 140, 1868
Zhao G.-B., Xia J.-Q., Li M., Feng B., Zhang X., 2005, Phys. Rev. D, 72, 123515
Zhao G.-B., Pogosian L., Silvestri A., Zylberberg J., 2009a, Phys. Rev. D, 79, 083513
Zhao G.-B., Pogosian L., Silvestri A., Zylberberg J., 2009b, Phys. Rev. Lett., 103, 241301
Zhao G.-B. et al., 2013, MNRAS, 436, 2038
Zhao G. et al., 2015, Advancing Astrophysics with the Square Kilometre Array (AASKA14), p. 165, available online at: http://pos.sissa.it/cgi-bin/reader/conf.cgi?confid=215-PLX6
Zhou X. et al., 2015, RAA, submitted
Zhu F., Padmanabhan N., White M., 2015, MNRAS, 451, 236
Zou H. et al., 2015, AJ, 150, 104

APPENDIX A: THE EXPLICIT FISHER MATRIX FOR THE DOUBLE-TRACER CASE

The Fisher matrix for a given $\boldsymbol{k}$ mode, $\mathcal{F}_{ij}(k, \mu)$ in equation (3), can be calculated explicitly as

$$\mathcal{F}_{ij}(k, \mu) = \mathcal{F}_{ij}^{\mathrm{AA}}(k, \mu) + \mathcal{F}_{ij}^{\mathrm{BB}}(k, \mu) + \mathcal{F}_{ij}^{\mathrm{X}}(k, \mu), \tag{A1}$$

where the Fisher matrices for tracers A, B and their cross-correlation X are

$$\mathcal{F}_{ij}^{\mathrm{AA}}(k, \mu) = \frac{1}{2} D_i^{\mathrm{A}} D_j^{\mathrm{A}} R_V^{\mathrm{AA}},$$

$$\mathcal{F}_{ij}^{\mathrm{BB}}(k, \mu) = \frac{1}{2} D_i^{\mathrm{B}} D_j^{\mathrm{B}} R_V^{\mathrm{BB}},$$

$$\mathcal{F}_{ij}^{\mathrm{X}}(k, \mu) = D_i^{\mathrm{X}} D_j^{\mathrm{X}} R_V^{\mathrm{XX}}$$
$$- \left(D_i^{\mathrm{X}} D_j^{\mathrm{A}} + D_i^{\mathrm{A}} D_j^{\mathrm{X}} \right) R_V^{\mathrm{XA}}$$

$$- \left(D_i^X D_j^B + D_i^B D_j^X \right) R_V^{XB}$$

$$+ \frac{1}{2} \left(D_i^A D_j^B + D_i^B D_j^A \right) R_V^{AB}. \tag{A2}$$

The derivative for the parameter p_i for tracer T is defined as

$$D_i^T = \frac{\partial \ln P_T}{\partial p_i}, \tag{A3}$$

where $T = \{A, B, X\}$. The power spectra and the effective volumes are

$$R_V^{AA} = \left[\frac{n_A P_A \left(1 + n_B P_B \right)}{\left(1 + n_A P_A \right) \left(1 + n_B P_B \right) - n_A n_B P_X^2} \right]^2,$$

$$R_V^{BB} = \left[\frac{n_B P_B \left(1 + n_A P_A \right)}{\left(1 + n_A P_A \right) \left(1 + n_B P_B \right) - n_A n_B P_X^2} \right]^2,$$

$$R_V^{XX} = \frac{n_A n_B \left[\left(1 + n_A P_A \right) \left(1 + n_B P_B \right) + n_A n_B P_X^2 \right]}{\left[\left(1 + n_A P_A \right) \left(1 + n_B P_B \right) - n_A n_B P_X^2 \right]^2} P_X^2,$$

$$R_V^{XA} = \frac{n_A^2 n_B \left(1 + n_B P_B \right)}{\left[\left(1 + n_A P_A \right) \left(1 + n_B P_B \right) - n_A n_B P_X^2 \right]^2} P_X^2 P_A,$$

$$R_V^{XB} = \frac{n_A n_B^2 \left(1 + n_A P_A \right)}{\left[\left(1 + n_A P_A \right) \left(1 + n_B P_B \right) - n_A n_B P_X^2 \right]^2} P_X^2 P_B,$$

$$R_V^{AB} = \frac{n_A^2 n_B^2 P_A P_B P_X^2}{\left[\left(1 + n_A P_A \right) \left(1 + n_B P_B \right) - n_A n_B P_X^2 \right]^2}. \tag{A4}$$

Let us consider several special cases.

(i) The single-tracer limit: $n_B = P_X \to 0$. In this case, only $\mathcal{F}_{ij}^{AA}(k, \mu)$ in equation (A2) is non-zero and it can be easily shown that it recovers the single-tracer result in equation (5), namely,

$$\mathcal{F}_{ij}(k, \mu) = \frac{1}{2} D_i^A D_j^A \left(\frac{n_A P_A}{1 + n_A P_A} \right)^2. \tag{A5}$$

(ii) The two independent-tracer limit: $P_X \to 0$. Only R_V^{AA} and R_V^{BB} are non-zero thus the total Fisher matrix is the sum of $\mathcal{F}_{ij}^{AA}(k, \mu)$ and $\mathcal{F}_{ij}^{BB}(k, \mu)$. It is easily shown that

$$\mathcal{F}_{ij}(k, \mu) = \frac{1}{2} D_i^A D_j^A \left(\frac{n_A P_A}{1 + n_A P_A} \right)^2$$

$$+ \frac{1}{2} D_i^B D_j^B \left(\frac{n_B P_B}{1 + n_B P_B} \right)^2. \tag{A6}$$

This is simply the result for two independent tracers.

(iii) The split-tracer limit: $P_A = P_B = P_X$, $n_A = n_B \to n_A/2$. This basically splits the same kind of tracer, say, tracer A, into two identical parts, so that the power spectra perfectly correlate with each other, and each subsample has one half of the total number of galaxies. In this case, all terms survive, and after some calculation, the final result turns out to be the same as the single tracer case,

i.e. equation (A5). This makes sense intuitively because two halves make one. A generalization also holds, say, if the same sample is arbitrarily split into two subsamples, the total Fisher matrix (with all the cross-correlation terms included) is the same as the original one without splitting.

[1]*National Astronomy Observatories, Chinese Academy of Science, Beijing 100012, China*

[2]*Institute of Cosmology and Gravitation, University of Portsmouth, Dennis Sciama Building, Portsmouth PO1 3FX, UK*

[3]*Center for Cosmology and Astro-Particle Physics, Ohio State University, Columbus, OH 43210, USA*

[4]*Institute for Gravitation and the Cosmos, The Pennsylvania University, University Park, PA 16802, USA*

[5]*Perimeter Institute for Theoretical Physics, Waterloo, Ontario N2L 2Y5, Canada*

[6]*Department of Physics and Astronomy, University of Utah, 115 S 1400 E, Salt Lake City, UT 84112, USA*

[7]*Laboratoire d'Astrophysique, Ecole polytechnique Fedérale de Lausanne, CH-1015 Lausanne, Switzerland*

[8]*Aix Marseille Université, CNRS, LAM (Laboratoire d'Astrophysique de Marseille) UMR 7326, F-13388 Marseille, France*

[9]*Department of Physics and Astronomy, University of Wyoming, Laramie, WY 82071, USA*

[10]*Instituto de Física Teórica, (UAM/CSIC), Universidad Autónoma de Madrid, Cantoblanco, E-28049 Madrid, Spain*

[11]*Department of Physics and Astronomy, University of British Columbia, Vancouver, BC V6T 1Z1, Canada*

[12]*Physics Department, Simon Fraser University, Burnaby, BC V5A 1S6, Canada*

[13]*Harvard-Smithsonian Center for Astrophysics, Cambridge, MA 02138, USA*

[14]*Departamento de Ciencias Fisicas, Universidad Andres Bello, Avda. Republica 220, Santiago, Chile*

[15]*Department of Physics and Astronomy and PITT PACC, University of Pittsburgh, 3941 O'Hara Street, Pittsburgh, PA 15260, USA*

[16]*CEA, Centre de Saclay, IRFU/SPP, F-91191 Gif-sur-Yvette, France*

[17]*Campus of International Excellence UAM+CSIC, Cantoblanco, E-28049 Madrid, Spain*

[18]*Instituto de Astrofísica de Andalucía (CSIC), Glorieta de la Astronomía, E-18080 Granada, Spain*

[19]*Department of Astronomy and Space Science, Sejong University, Seoul 143-747, Korea*

[20]*Department of Astronomy and Astrophysics, The Pennsylvania State University, University Park, PA 16802, USA*

[21]*Department of Physics and Astronomy, Ohio University, 251B Clippinger Labs, Athens, OH 45701, USA*

[22]*Centre de Physique des Particules de Marseille, CNRS/IN2P3-Luminy and Université de la Méditerranée, Case 907, F-13288 Marseille Cedex 9, France*

[23]*Department of Physics and Tsinghua Center for Astrophysics, Tsinghua University, Beijing 100084, China*

[24]*Department of Physics, Yale University, New Haven, CT 06511, USA*

This paper has been typeset from a TeX/LaTeX file prepared by the author.